Electronic Supplementary Material (ESI) for Nanoscale Advances.

Understanding the thermal conductivity variations in nanoporous anodic aluminum oxide

Liliana Vera-Londono[1], Alejandra Ruiz-Clavijo[1], Olga Caballero-Calero[1],

Marisol Martín-González[1,*]

[1] Instituto de Micro y Nanotecnología, IMN-CNM, CSIC (CEI UAM+CSIC) Isaac Newton, 8, E-28760, Tres Cantos, Madrid, Spain

E-mail: marisol.martin@csic.es

Supporting information

Table SI: Thermal conductivity values (k) obtained for the different samples.

Table SII: Porosity, interpore distance and pore diameter of the different AAOs after annealing treatments.

Calibration of the 3ω-SThM (Including Figure S1)

Inner and outer layers (Including Figures S2 and S3)

Figure S4: Density measurement of the skeletal AAO-membranes after annealing treatments.

Table S.I: Thermal conductivity (k) values obtained for the different samples. The error shown in the table comes from the dispersion of the data analysis of several measurements. The error in the thermal conductivity measurement is less than 20%.

Temperature (ºC)	***k*** **Sulfuric-AAOs**	***k*** **Oxalic-AAOs**	***k*** **Phosphoric-AAOs**
25	1.24±0.12	1.41±0.17	1.44±0.13
50	1.09±0.18	1.34±0.16	1.31±0.15
100	0.78±0.19	1.26±0.24	1.36±0.11
150	1.15±0.24	1.35±0.22	1.22±0.17
200	1.33±0.26	1.67±0.24	1.55±0.13
600	1.85±0.28	1.96±0.35	2.04±0.22
950	2.99±0.23	3.43±0.28	2.48±0.38
1100	3.84±0.33	4.46±0.32	3.24±0.38
1300	4.16±0.35	4.82±0.36	3.38±0.32

Table S.II. Porosity and pore diameter of the different AAOs after temperature annealing.

Samples	**Sulfuric-AAO**			**Oxalic-AAO**			**Phosphoric-AAO**		
Heat treat. (º C)	~Ø pore (nm)	Poros. (%)	Interp. dist. (nm)	~Ø pore (nm)	Poros. (%)	Interp. dist. (nm)	~Ø pore (nm)	Poros. (%)	Interp. dist. (nm)
25	19	8	64	28	7	103	217	34	329
50	19	8	64	28	7	105	221	38	304
100	20	9	65	30	8	104	215	36	301
150	20	9	64	34	10	102	-	-	-
200	19	9	63	33	9	102	220	36	303
600	23	12	64	33	10	102	216	34	314
950	23	12	64	37	12	102	241	39	309
1100	28	18	64	48	20	101	229	37	325

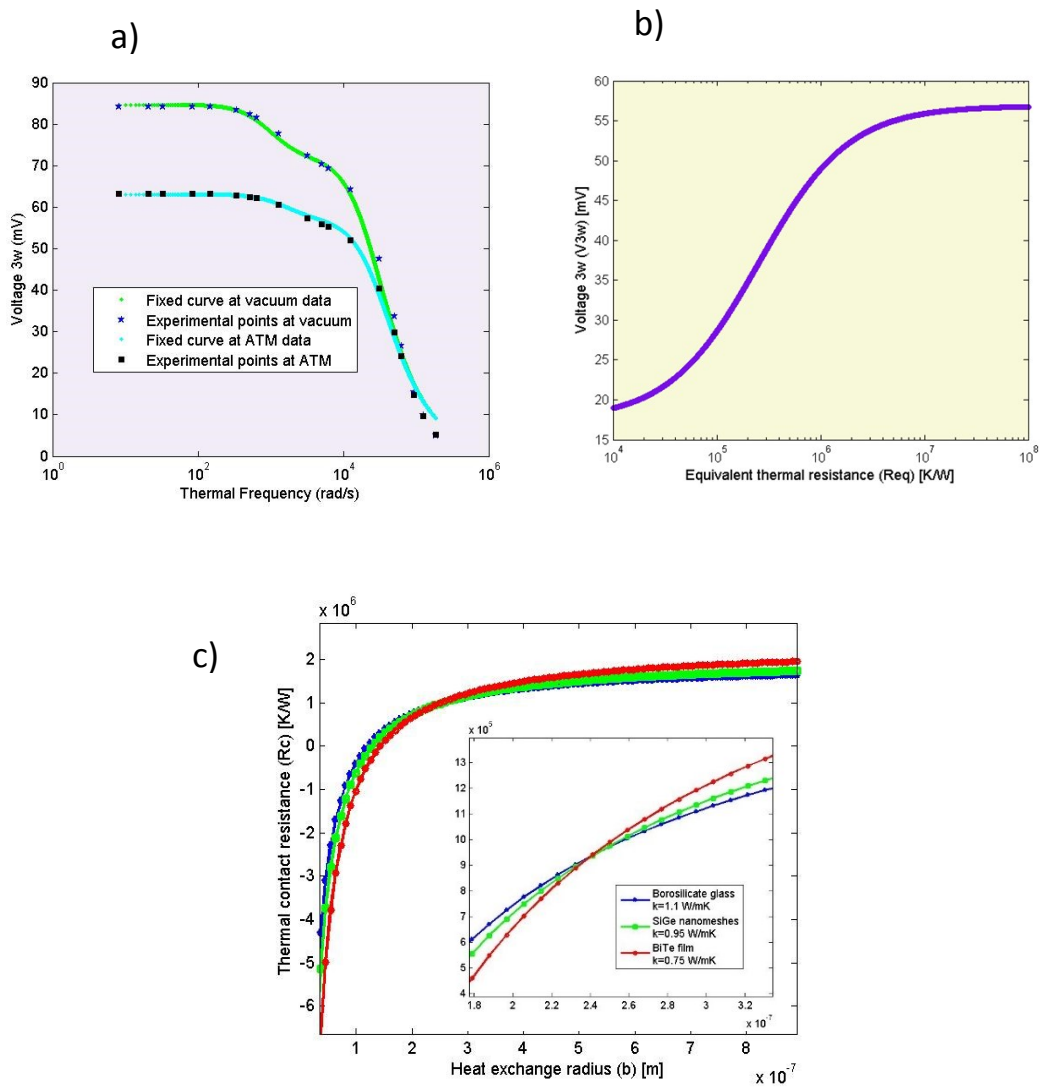

Figure S1: Calibration curves for the 3ω-SThM performed for the measurements shown in the paper.

In brief, the 3ω-SThM technique involves certain calibration processes of the AFM tip to be used before the actual measurements, as described in references [a, b] to determine the heat exchange radius (b) and the equivalent thermal resistance (R_{eq}) between the tip and the sample. To perform this calibration, the first step is to take measurements in a high vacuum (10^{-5} mbar) and ambient to obtain the 3ω response of the AFM tip at different frequencies (Figure S1.a). To obtain this curve, the experimental probe response of $V_{3\omega}$ as a function of frequency was fixed by a model implemented in Matlab, using well known geometrical and physical parameters of the probe, and setting other parameters in the code. As a result of these adjustment parameters, the curves for

vacuum and ambient conditions for the thermal response of the probe were respectively fixed, as is shown in the figure of supporting information (S1a). A third curve (S2) relates the $V_{3\omega}$ response with an equivalent thermal resistance in the probe-to-sample configuration. The fourth code is running to obtain a cross-point curve, as was reported in [a]. In this case, the previous parameters used for setting the thermal probe response in vacuum and air, are used to fix a new curve along with the V3ω response for different calibration samples. The thermal conductivity values of the calibration samples should very well know. In this case, the samples were analyzed in a previous robust system as is the photoacoustic technique, to ensure an accurate thermal conductivity value in the model. The different reference samples measured were, in this case, borosilicate glass, SiGe nanomeshes [c], and a Bi_2Te_3 film grown by electrochemistry. Taking into account that their thermal conductivity values are well known (1.1, 0.95, and 0.75 W/m·K, respectively), these curves (shown in Figure S1.c) are used to obtain the cross point between b and R_c, which is the contact resistance. This last curve provides information about the heat flux thermal exchange radius and the thermal contact resistance. These values will be then fixed for this AFM tip and used for the subsequent measurements.

Then, the thermal conductivity of the composite can be obtained from the measurements applying Equation S1:

$$R_s^{th} = (4 \cdot b \cdot k_{comp})^{-1} \qquad \textit{Equation S1}$$

, where R_s^{th} is the sample's thermal resistance (obtained from R_{eq} and R_c), k_{comp} is the thermal resistance of the composite. In this experiment, the thermal conductivity was obtained using active mode at constant current and under ambient conditions. Usually, the current is around 0.60 mA to 1.30 mA. In this case, the applied current was 1.08 mA.

Finally, using semi-infinite medium assumption (Equation S2), we extract the composite thermal conductivity (k_{comp}) and we use this value in the Effective Medium Theory,

$$k_{comp} = p \cdot k_{air} + (1-p)\, k_{AAO}, \qquad \textit{Equation S2}$$

, where p and k_{air} are the porosity and thermal conductivity of the air, to finally obtain the effective thermal conductivity of AAO, k_{AAO}.

Inner and outer layers:

It is also worth noting that the presence of impurities is higher in the outer-pore layer than in the inner-pore layer. As it has been reported, this inner pure region could be in the order of 40 nm for phosphoric-AAO, 20 nm for oxalic-AAO, and 10 nm for sulfuric-AAO. In figure 2 different regions in the thermal images were detected, with different 3ω voltages. Although the resolution of our tip is in the limit of the inner pore size, it is possible to observe some thermal contrasts in the surface's AAO when the thermal and topographic profiles are compared (see Figure S2 in Supporting Information). There, it can be seen a lower thermal conductivity in the region surrounding the pores. This proves, for the first time, local thermal differences in the outer AAO region, where the incorporated species from the acid solution are responsible for decreasing the thermal flux. In our case, the effective medium theory (see Supporting Information) has been used to determine the effective thermal conduction without air contribution, and thus take into account those different parts of the AAO-template structure.

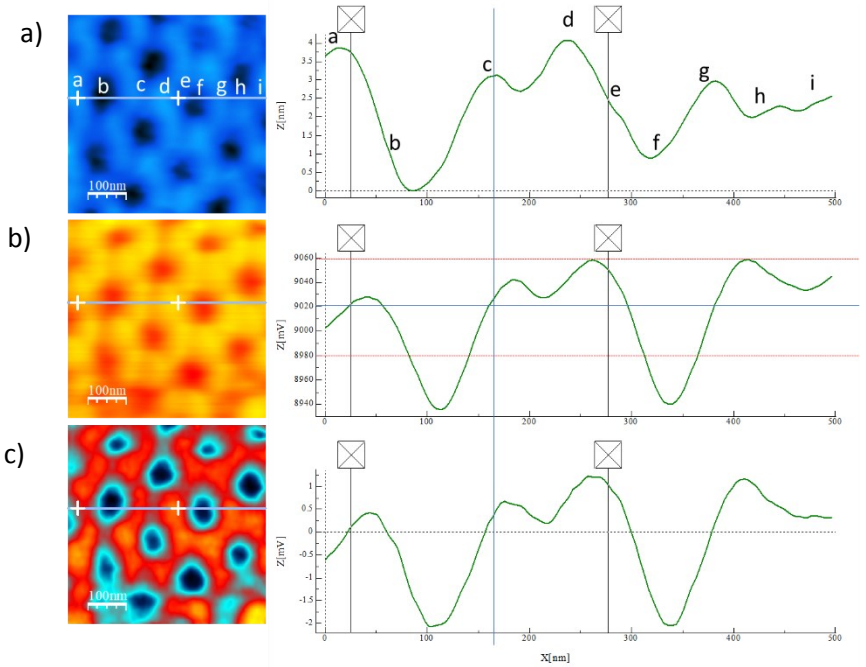

Figure S2: Topographic image and profile found in a). Thermal images and profiles of (3ω) in b) and (1ω) in c). The letters in the profiles are indicating the fluctuation in the thermal information in respect to the topographic features. In e and h points in the profiles, it can be observed how regions near to outer pore in the topographic AAO image, have an increase in 3ω voltage, meaning a lower thermal conductivity value.

In our case, the resulting heat exchange radius, *b*, was of 250 nm and taking into account the topography of the samples, the use of the effective medium theory is fully justified. Then, the following figure S3 shows different data obtained for topography and thermal signal are presented. The correlation between both signals is not always the same, which means that the thermal image is real and does not depend on the morphology of the sample. Moreover, the thermal conductivity is obtained from the 3ω signal, obtaining the mean value, as it was explained before. It is also interesting to see that, for the oxalic sample, the difference in the values for RT and 100ºC annealing can be seen.

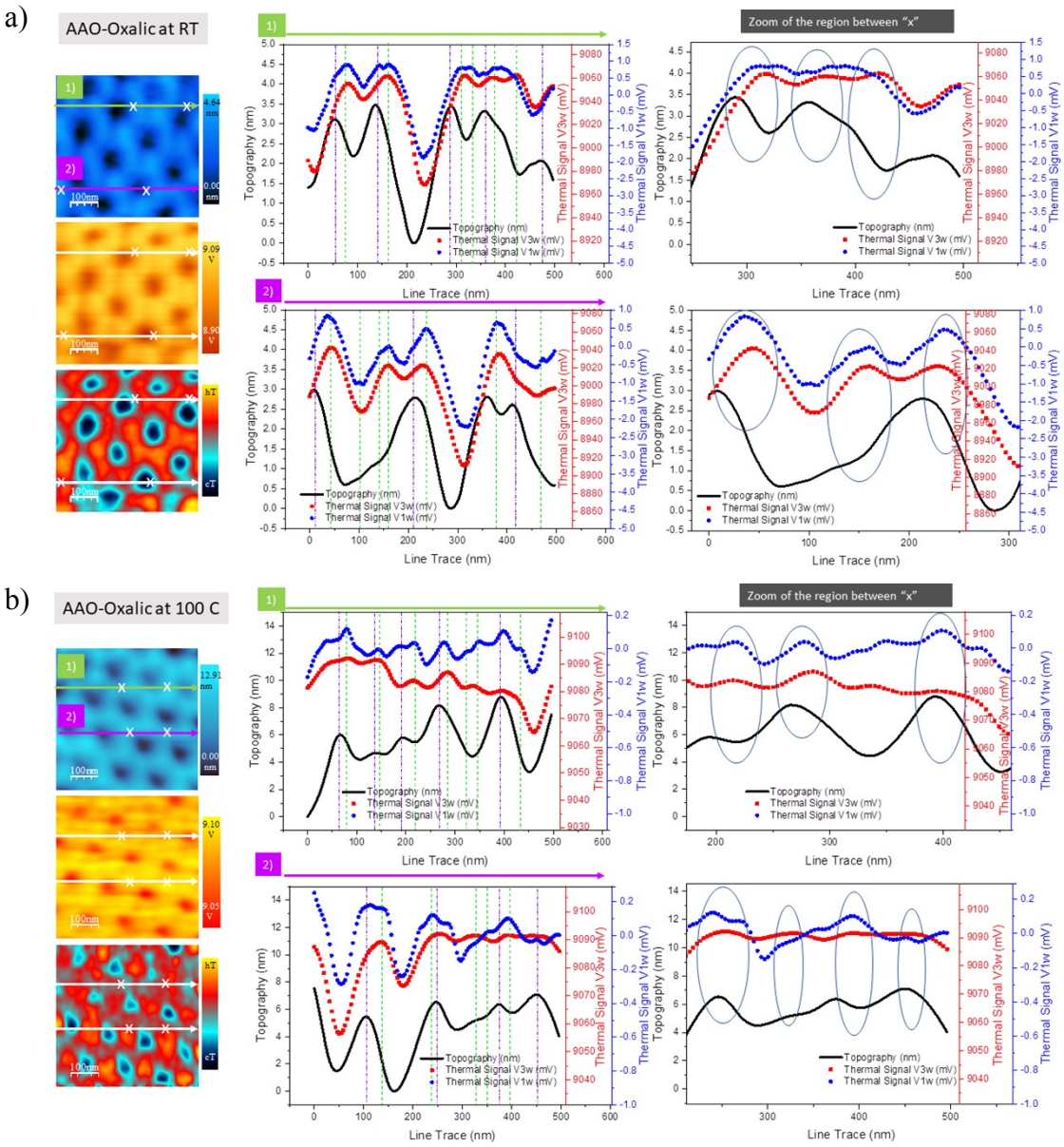

c)

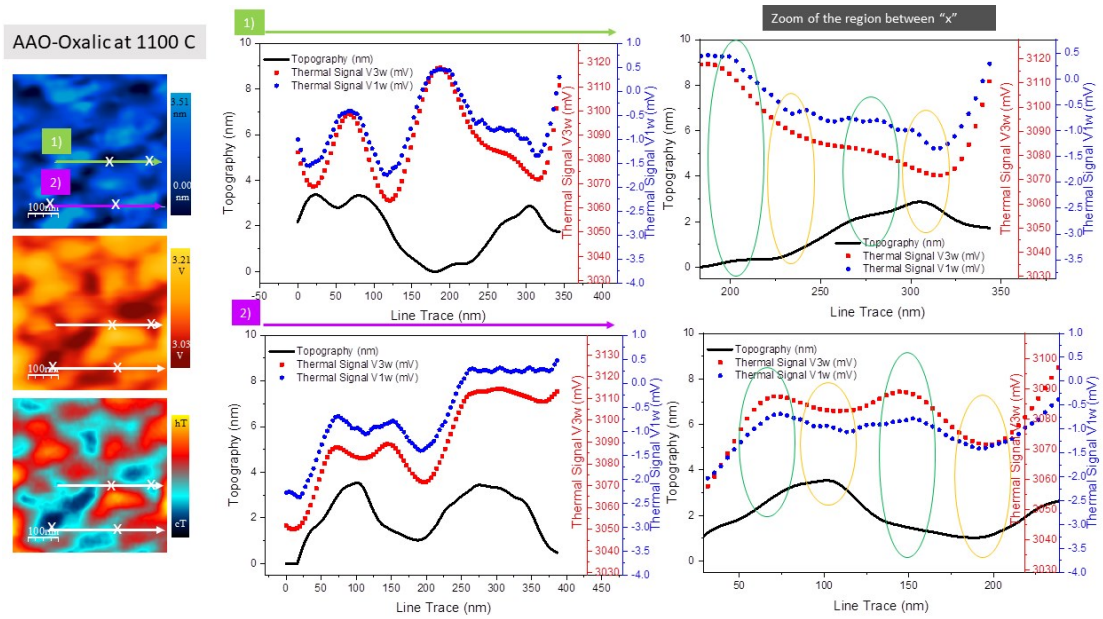

d)

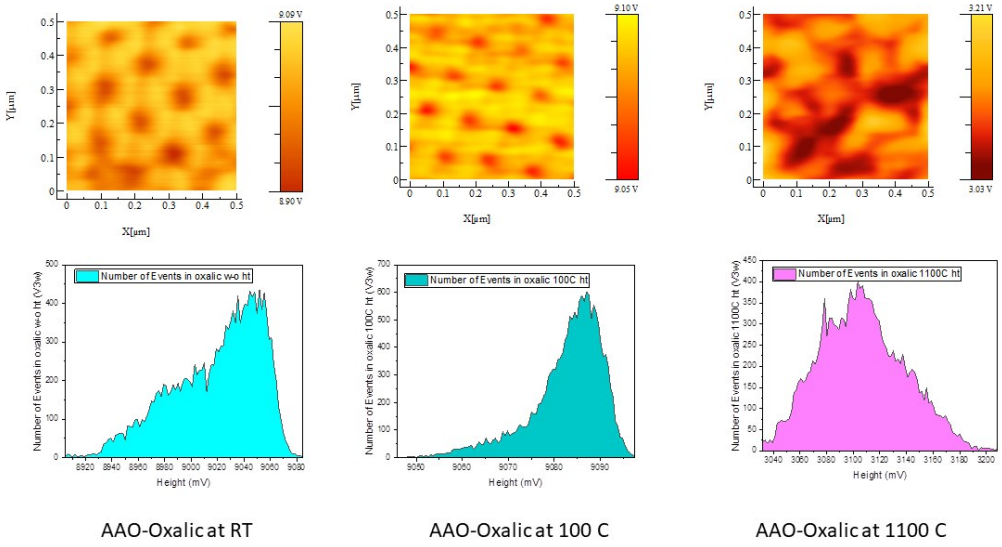

Figure S3: a), b), and c) show the data obtained for the a) oxalic-AAO at RT, b) oxalic-AAO annealed at 100ºC, and oxalic-AAO annealed at 100'ºC. Each of these figures is organized as follows: left up, topographical image, left middle, 1ω-signal, left bottom 3ω-signal. Then, d) shows the thermal image (up) and the histograms of the values in mV obtained in the measurement (down) of the samples, from left to right, of the sample at RT, annealed at 100º C and annealed at 1100ºC. Here, the differences in the values from RT and 100ºC are shown.

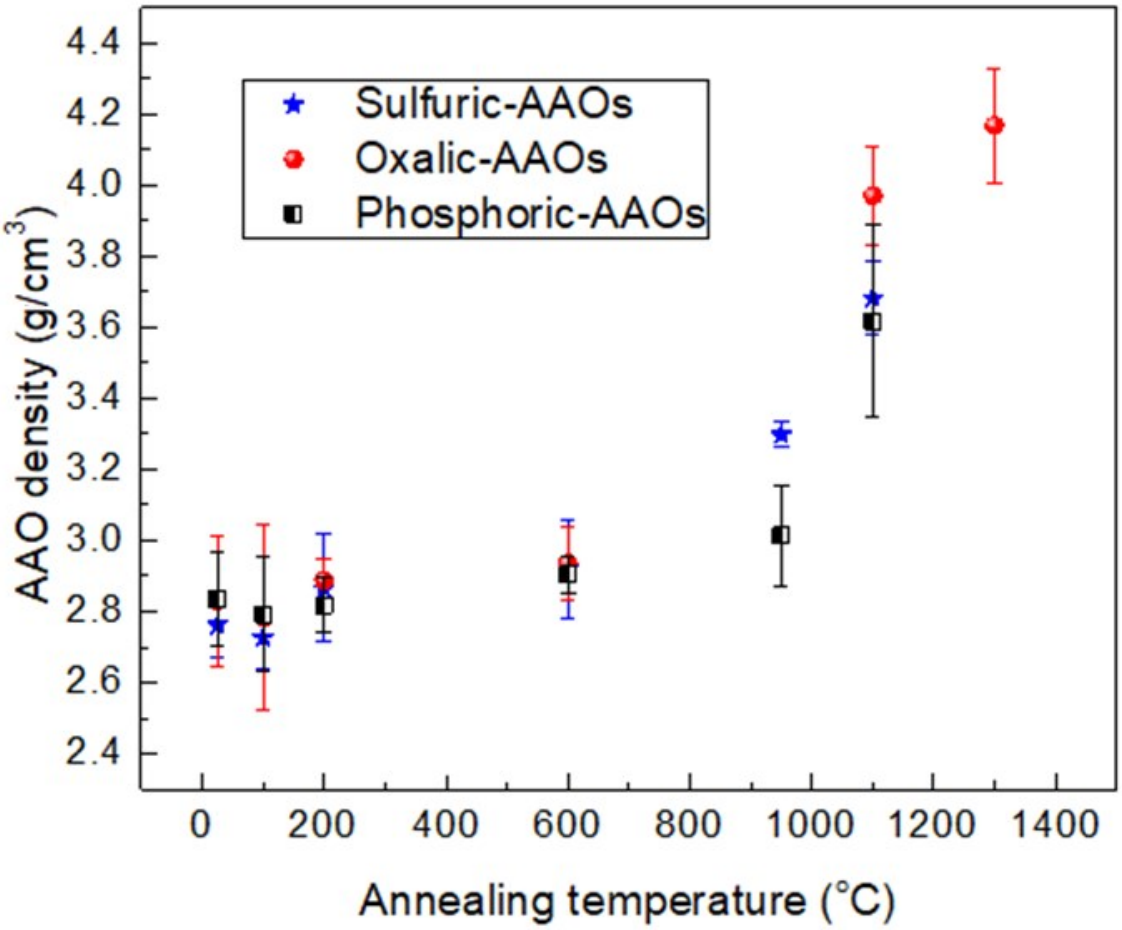

Figure S4: Density measurements of the skeletal AAO-membranes after annealing performed by the Archimedes' method.

References Supporting Information

[a] A. A. Wilson, M. M. Rojo, B. Abad, J. A. Perez, J. Maiz, J. Schomacker, M. Martín-Gonzalez, D.-A. Borca-Tasciuc, and T. Borca-Tasciuc, Nanoscale **7**, 15404 (2015).
[b] Vera-Londono, L., et al., Advances in Scanning Thermal Microscopy Measurements for Thin Films, in Coatings and Thin-Film Technologies. 2018, IntechOpen.
[c] J. A. Perez-Taborda, M. M. Rojo, J. Maiz, N. Neophytou, and M. Martin-Gonzalez, Scientific Reports **6**, 32778 (2016).